*Biochimica et Biophysica Acta*, 764 (1984) 253–271
Elsevier



BBA 41453

# ELECTRONIC INTERACTIONS BETWEEN IRON AND THE BOUND SEMIQUINONES IN BACTERIAL PHOTOSYNTHESIS

## EPR SPECTROSCOPY OF ORIENTED CELLS OF *RHODOPSEUDOMONAS VIRIDIS* *

G. CHARLES DISMUKES [a], HARRY A. FRANK [b], RICHARD FRIESNER [c,**] and KENNETH SAUER [c]

[a] *Department of Chemistry, Princeton University, Princeton, NJ 08544;* [b] *Department of Chemistry, University of Connecticut, Storrs, CT 06268; and* [c] *Department of Chemistry, University of California and the Chemical Biodynamics Division, Lawrence Berkeley Laboratory, Berkeley, CA 94720 (U.S.A.)*

(Received July 4th, 1983)

*Key words: Bacterial photosynthesis; ESR; Electron transport; Iron-semiquinone; (Rps. viridis)*

**Electron paramagnetic resonance (EPR) spectroscopy of the iron-semiquinone complex in photosynthetic bacterial cells and chromatophores of *Rhodopseudomonas viridis* is reported. Magnetic fields are used to orient the prolate ellipsoidal-shaped cells which possess a highly ordered internal structure, consisting of concentric, nearly cylindrical membranes. The field-oriented suspension of cells exhibits a highly dichroic EPR signal for the iron-semiquinone complex, showing that the iron possesses a low-symmetry ligand field and exists in a preferred orientation within the native reaction-center membrane complex.The EPR spectrum is analyzed utilizing a spin hamiltonian formalism to extract physical information describing the electronic structure of the iron and the nature of its interaction with the semiquinones. Exact numerical solutions and analytical expressions for the transition frequencies and intensities derived from a perturbation theory expansion are presented, and a computer-simulated spectrum is given. It has been found that, for a model which assumes no preferred orientation within the plane of the membranes, the orientation of the $Fe^{2+}$ ligand axis of largest zero-field splitting ($Z$, the principal magnetic axis) is titled $64 \pm 6°$ from the membrane normal. The ligand field for $Fe^{2+}$ has low symmetry, with zero-field splitting parameters of $|D_1| = 7.0 \pm 1.3$ $cm^{-1}$ and $|E_1| = 1.7 \pm 0.5$ $cm^{-1}$ and $|E_1/D_1| = 0.26$ for the redox state $Q_1^- Fe^{2+} Q^{2-}$. The rhombic character of the ligand field is increased in the redox state $Q_1 Fe^{2+} Q_2^-$, where $0.33 > |E_2/D_2| > 0.26$. This indicates that the redox state of the quinones can influence the ligand field symmetry and splitting of the $Fe^{2+}$. There exists an electron-spin exchange interaction between $Fe^{2+}$ and $Q_1^-$ and $Q_2^-$, having magnitudes $|J_1| = 0.12 \pm 0.03$ $cm^{-1}$ and $|J_2| \simeq 0.06$ $cm^{-1}$, respectively. Such weak interactions indicate that a proper electronic picture of the complex is as a pair of immobilized semiquinone radicals having very little orbital overlap (probably fostered by superexchange) with the $Fe^{2+}$ orbitals. The exchange interaction is analyzed by comparison with model systems of paramagnetic metals and free radicals to indicate an absence of direct coordination between $Fe^{2+}$ and $Q_1^-$ and $Q_2^-$. Selective line-broadening of some of the EPR transitions, involving $Q^-$ coupling to the magnetic sublevels of the $Fe^{2+}$ ground state, is interpreted as arising from an electron-electron dipolar interaction. Analysis of this line-broadening indicates a distance of 6.2–7.8 Å between $Fe^{2+}$ and $Q_1^-$, thus placing $Q_1$ outside the immediate coordination shell of $Fe^{2+}$.**

* This article is dedicated to the memory of Betty J. Clayton.

** Present address: Department of Chemistry, University of Texas, Austin, TX, U.S.A.

Abbreviation: EXAFS, extended X-ray absorption fine structure.

## Introduction

A wide range of evidence supports the involvement of two protein-bound quinone molecules as consecutive electron acceptors in the secondary electron transfer steps of photosynthesis in purple bacteria [1]. In intact cells and chromatophore membrane fractions electron transfer from the reduced primary quinone, $Q_1^-$, to the second quinone, $Q_2$, occurs in the presence of a nearby Fe ion [1–3]. The functional role of Fe is unclear. It has been postulated that it may be involved in: (a) determining the redox potentials and proton binding of the quinone/semiquinone couple; (b) facilitating electron transfer between the quinones by direct orbital overlap; (c) a simple structural role in binding subunits of the reaction-center protein complex, which is the smallest photochemically active component which carries out the initial electron transfer steps; (d) and others (reviewed in Refs. 4 and 5).

Low-temperature EPR [6], magnetic susceptibility [7], and Mössbauer studies on reaction centers of *Rhodopseudomonas spheroides* (R-26, carotenoidless mutant) [8,9] have shown that there is a weak electron exchange interaction between Fe and $Q_1^-$. Both $Q_1$ and $Q_2$ are ubiquinones in this bacterium. In reaction centers of the same organism in which the detergent solubilized $Q_2$ is reconstituted [10,11] and in whole cells [12], chromatophores [13] and reaction centers [14] of *Rhodopseudomonas viridis*, the EPR spectrum recorded under conditions where $Q_2$ is reduced by one electron is qualitatively similar to that for $Q_2^-$Fe, although the linewidths differ. $Q_1$ is a menaquinone in *Rps. viridis* [15]. It is concluded from these data that the electron spin exchange interaction between iron and both semiquinones is comparable in magnitude. Evidently, the iron is not essential for the $Q_1^-Q_2$ to $Q_1Q_2^-$ electron transfer in reaction centers of *Rps. spheroides* (R-26), since it has been shown that biosynthetic replacement of $Fe^{2+}$ by $Mn^{2+}$ does not alter the kinetics of this step (Nam, H., Austin, R.A. and Dismukes, G.C., unpublished data). Steady-state Mössbauer experiments on unreduced reaction centers have shown that the oxidation state of Fe is +2 with a high spin electronic ground state. Also, magnetic susceptibility indicates that the symmetry and strength of the Fe ligand field remains unchanged upon reduction of $Q_1$ [8,9].

The structure of the complex between Fe and the semiquinones is unknown. EXAFS (extended X-ray absorption fine structure) experiments indicate that there is no apparent change in Fe ligand distances or coordination number upon reduction of the quinones or upon addition of inhibitors [16,17]. The various spectroscopic results are consistent in the observation of a weak or non-detectable interaction between Fe and both semiquinones. This supports a location of the quinones outside the first coordination sphere of the Fe.

In this paper we present new results on the iron-semiquinone EPR properties in oriented samples of *Rps. viridis*. Because of the existence of a highly ordered internal membrane structure, oriented cells exhibit a large EPR dichroism. A quantitative analysis of the EPR spectrum is given.

## Materials and Methods

*Sample preparation.* Cells of *Rps. viridis* were grown by the method of Eimhjellen et al. [18]. Cells were harvested by centrifugation at $7000 \times g$, followed by washing in 0.025 M Tris buffer (pH 7.5) and stored at −20°C if not used immediately. Chromatophores were prepared by passage of cells through a French press at 20000 lb/inch$^2$, followed by a low-speed centrifugation to remove unbroken cells and cell-wall material.

Whole cells of *Rps. viridis* are shaped like irregular prolate ellipsoids which align in magnetic fields with the long axis of the cell perpendicular to the applied field [19–22]. Cells treated as discussed below were permanently oriented by freezing to −75°C in Suprasil quartz tubes of $3 \times 4$ mm bore in the presence of a 21 kG magnetic field. The extent of orientation of the cells at 21 kG is near the saturation limit observed at higher fields. The intracellular membranes within *Rps. viridis* form cylindrical shaped sheets concentric with one another and having the cylinder axis, $\boldsymbol{L}$, colinear with the long axis of the bacterium [23]. Because the long axis of the bacteria aligns with a uniform distribution in the plane perpendicular to the 21 kG field, as indicated by the arrow in Fig. 1, EPR measurements can be made either perpendicular to or within the plane defined by the

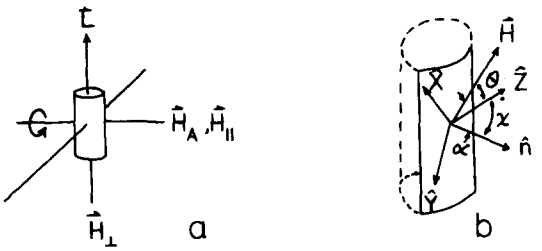


Fig. 1. (a) The orientation of the long axis of the bacterial cells ($\boldsymbol{L}$) relative to the magnetic field used to induce orientation $\boldsymbol{H}_A$ is shown. The intracellular membranes in *Rps. viridis* occur as nested sets of cylindrical membrane sheets for which the cylinder axis is colinear with $\boldsymbol{L}$. After freezing the cells, the magnetic field needed for EPR may be made parallel, $\boldsymbol{H}_{||}$, or perpendicular, $\boldsymbol{H}_\perp$, to the alignment direction. (b) A definition of the axes used to describe the orientation of the EPR Zeeman field, $\boldsymbol{H}$, and the membrane normal, $\hat{n}$, is given in terms of the principal axis system of the zero-field splitting tensor of the $Fe^{2+}(\hat{X}, \hat{Y}, \hat{Z})$. $\theta = \cos^{-1}(\boldsymbol{H}\cdot\hat{Z})$, $\chi = \cos^{-1}(\hat{Z}\cdot\hat{n})$ and $\alpha = \cos^{-1}(\boldsymbol{H}\cdot\hat{n})$.

long axis of the bacteria. This permits measurement of EPR spectra with the Zeeman field preferentially out-of-plane ($\boldsymbol{H}_{||}$) or preferentially in-plane ($\boldsymbol{H}_\perp$) relative to the surface of the intracellular membranes, respectively.

Whole cells and chromatophores were suspended in one of two solutions of different redox potentials. Mild reducing conditions were provided by vortex mixing of the wet sample paste with an equal volume of buffer comprising 0.025 M glycine/0.1 M KCl/0.01 M sodium ascorbate/ $10^{-5}$ M phenazine methosulfate at pH 10. The concentrations refer to the final concentrations of the mixture after addition of 50% glycerol (v/v) immediately prior to freezing or illumination. Strong reducing conditions were provided by the same buffer except that 0.01 M sodium dithionite replaced ascorbate, $10^{-5}$ M methyl viologen replaced phenazine methosulfate, and the mixing was done under $N_2$ gas. Samples were kept in the dark following this treatment.

Illumination with a water-filtered tungsten lamp was used on some samples to promote photoreduction of reaction-center acceptors and equilibrium with the added redox agents. Dark-adapted samples were then incubated for 5 min on ice prior to freezing.

EPR measurements were carried out by conventional methods using a Varian E-9 or E-12 spectrometer with 100 kHz magnetic-field modulation and a gaseous helium cryostat. Both rectangular TE-102 and cylindrical TE-110 microwave cavities were used in these studies.

*EPR simulation.* Computer simulations of the EPR spectra were performed by use of numerical solutions of the appropriate spin hamiltonian given in the next section. The numerical method for matrix diagonalization employed the routines VCVTCH and EIGCH within the International Mathematical Society Library of routines available from Argonne National Laboratory [24]. Explicit evaluation of the matrix elements on the symmetrized direct product basis functions is given in Appendix A. The simulations were conducted assuming a static resonance field of 3270 G ($\boldsymbol{H}_0$).

New eigenvalues and transition intensities were calculated for every 4.5° increment in $\theta$ and $\phi$, and summed over a $\pi/2$ quadrant for each, using an appropriate distribution function for the alignment of cells. The accuracy of this finite increment was checked by conducting simulations using a finer increment. No significant lineshape changes were observed. The orientation dependence of the transition probability was explicitly calculated in all cases. A general expression for the transition matrix element for an arbitrary eigenfunction expressed in terms of the ten basis functions was derived (Appendix B).

The parameters of the spin hamiltonian were explicitly surveyed over the range $1.85 \leqslant |D| \leqslant 8.75$ $cm^{-1}$; $0.60 \leqslant |E| \leqslant 2.9$ $cm^{-1}$; $|E/D| \leqslant \frac{1}{3}$; $2.3 \leqslant |g_{Fe}| \leqslant 1.7$; $g_Q = 2.0$; $0.037 \leqslant |J| \leqslant 0.23$ $cm^{-1}$. A good fit was judged by three criteria: first, the ability to reproduce the positions of the features at 'effective' $g'$ values of approx. 1.84 and approx. 1.65 *, second, the ability to predict the correct relative intensities at these effective $g'$ values. The final condition for a suitable simulation was the prediction of the narrow linewidth of the 1.84 peak and the 'nub' between the 1.84 and 1.65 peaks. In the case of aligned cells, the angle dependence of the integrated $Q^-Fe^{2+}$ signal for parallel vs. perpendicular orientations was also a constraint for a successful simulation.

* See legend to Fig. 6 for definition of $g'$.

The orientational distribution function which describes the combined spread in alignment of the bacteria, the internal membranes and the paramagnetic center was assumed to be identical to that found using the spin-polarized triplet state, $^3$P-960, as a probe of the extent of orientation [19]. This result shows a gaussian distribution for the angle between the alignment field and the bacterium with a width (in radians) of $\Delta = 0.40$ for an aligning field strength of 21 kG.

## Theory

To understand the origin of the EPR spectrum we conducted a computer simulation of the spectrum derived from diagonalization of an appropriate spin hamiltonian. The suitability of the spin hamiltonian approach is generally accepted when the ground electronic state is well separated in energy from excited electronic states compared to the matrix elements which couple these states. These are typically due to spin-orbit interactions. The identity, number and symmetry of the ligands about the iron are not known at present, nor are the energies of the excited ligand field states. The spin hamiltonian approach has been examined by Butler et al. [7] and found to be successful in predicting the magnetic susceptibility of $Q^-Fe^{2+}$. These authors examined the case of a six-coordinate $Fe^{2+}$ with rhombic distortion.

Prediction of the EPR spectral properties was performed using the hamiltonian in Eqn. 1 for the calculation of the energy levels for $Q^-Fe^{2+}$ assuming only the lowest orbital-singlet spin-quintet ground state for $Fe^{2+}$ to be populated:

$$\mathcal{H} = \beta \boldsymbol{H} \cdot \hat{g}_{Fe} \cdot \boldsymbol{S}_{Fe} + g_Q \beta \boldsymbol{H} \cdot \boldsymbol{S}_Q + D\left[S_z^2 - \tfrac{1}{3}S(S+1)\right]_{Fe} + E\left(S_x^2 - S_y^2\right)_{Fe} + J\boldsymbol{S}_{Fe} \cdot \boldsymbol{S}_Q \quad (1)$$

This includes an anisotropic $g$-tensor for the iron having the spin vector $\boldsymbol{S}_{Fe}$, and components $S_x$, $S_y$ and $S_z$ (the subscript Fe is suppressed for notational clarity), an isotropic $g$ value for one semiquinone having spin vector $\boldsymbol{S}_Q$, zero-field splitting of the iron ground state including axial ($D$) and orthorhombic ($E$) field components, and an isotropic Heisenberg spin-exchange interaction ($J$). Electron spin dipole–electron spin dipole coupling and an anisotropic exchange interaction were not explicitly included, because the magnitude of these interactions is expected to be at least an order of magnitude smaller than any term in Eqn. 1. The expected magnitude of the anisotropic exchange interaction is approximately $(\Delta g/g)^2 J$ [25]. The estimated maximum $g$-anisotropy for $Fe^{2+}$ in the reaction centers of *R. spheroides* is approx. $\Delta g = 0.15$ [7], which gives an estimate for the maximum anisotropic exchange of 0.02 J. Dipolar broadening is treated in Appendix D.

Evaluation of the spin hamiltonian (Eqn. 1) on the ten-dimensional symmetrized direct-product basis states [26] for $Q^-Fe^{2+}$ yields the matrix elements given in Appendix A. Numerical integration, as described in the Materials and Methods section, yields a set of eigenvalues and eigenvectors for a fixed magnetic field strength ($H_0$) and a

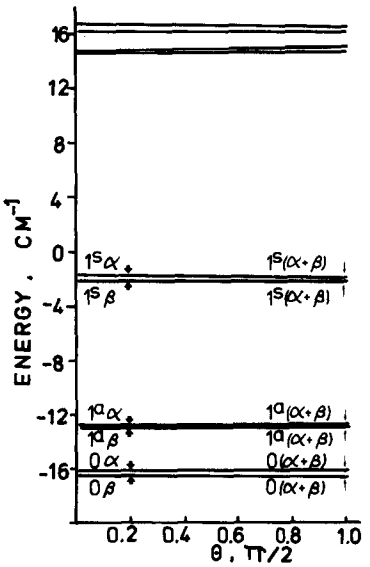


Fig. 2. Energy-level diagram as a function of the angle, $\theta$, between $\boldsymbol{H}$ and the principal magnetic axis, $\hat{z}$, for $Q^-Fe^{2+}$. The parameters for this illustration are $D = 7.75$ cm$^{-1}$, $E = 1.87$ cm$^{-1}$, $|E/D| = 0.24$, $J = 0.13$ cm$^{-1}$, $g_Q = 2.00$, $g_\parallel = 2.00$, $g_\perp = 2.10$, $H_0 = 3200$ G and $\phi = 0$. The six lowest states give rise to the $X$-band EPR transitions observed below 20 K. Each is labelled by the direct product spin function which appears with the largest coefficient in the eigenfunction found by solving hamiltonian (Eqn. 1). These wavefunctions are orientation dependent. The width of the arrows indicates the relative oscillator strength.

fixed set of angles $\theta$ and $\phi$. An energy level diagram as a function of the angle $\theta$ between the principal magnetic axis, $\hat{Z}$, and the applied magnetic field is given in Fig. 2 for $\phi = 0$, using parameters fit to Eqn. 1. The eigenvalues are admixtures of all ten basis functions; however, usually one or two basis states predominate. As noted in the figure, there is a major change in the $Q^-$ part of the wave-functions with $\theta$, and this is the origin of the orientation dependence of the integrated intensity (vide infra).

Transition probabilities between initial and final state eigenvectors were calculated using Eqn. 2:

$$W_{if}(\theta, \phi) = \frac{1}{\hbar^2} |\langle i | \boldsymbol{H}_1 \cdot \hat{g} \cdot \boldsymbol{S} | f \rangle|^2 \tag{2}$$

When expressed in terms of the principal axis system of the iron (Fig. 1) this involves (for no hyperfine interaction):

$$\boldsymbol{H}_1 \cdot \hat{g} \cdot \boldsymbol{S} = H_1 \{ \cos\theta [\cos\phi (g_Q S_Q + g_{Fe} S_{Fe})_z + \sin\phi (g_Q S_Q + g_{Fe} S_{Fe})_y] + \sin\phi (g_Q S_Q + g_{Fe} S_{Fe})_z \} \tag{3}$$

A general expression for $W_{if}$ for the ten eigenvectors was derived and is presented in Appendix B. All transitions falling within the $x$-band frequency region were computed and weighted by a gaussian linewidth function, $g(\nu)$, and scaled by the Boltzmann probability function, $P_i = \exp(-E_i/\boldsymbol{k}T)/Z$, (with $Z$ = partition function for the ten magnetic states) to obtain the intensity at a particular $\theta$ and $\phi$:

$$I_{if}(\theta, \phi) = W_{if}(\theta, \phi) g(\nu) P_i(E_i, T) \tag{4}$$

The resonant field position of this transition, $H_{if}$, was obtained by relating it to the transition energy obtained from the diagonalization. This yields Eqn. 5 for the field position of the transition relative to the fixed-field strength, $H_0$, used in the diagonalization:

$$H_{if} - H_0 = (h\nu - E_{if})/g'\beta \tag{5}$$

The transition probability for the $i \rightarrow f$ transition integrated over all possible orientations for a randomly oriented ensemble of cells includes the weighting factor, $\sin\theta$, which accounts for the greater probability that $H$ will be perpendicular to the $Z$ zero field splitting axis rather than parallel to it:

$$I_{if}(H) = \int_0^{2\pi} \int_0^{\pi} I_{if}(\theta, \phi) \sin\theta \, d\theta \, d\theta \tag{6}$$

The total observed signal for all transitions is then:

$$I(H) = \sum_{i<f=1}^{10} I_{if}(H) \tag{7}$$

Only those occurring in the $x$-band region were considered.

*EPR simulation in aligned cells*

To obtain the expression analogous to Eqn. 6 for the case of a magnetically oriented distribution of cells, it is necessary to relate the essentially fixed orientation of the zero field splitting axes for $Fe^{2+}$ to the distribution function, describing the orientation of the cells in the aligning field [27]. Referring to Fig. 1b, we need the probability that the Zeeman field, $\boldsymbol{Z}$, makes an angle $\alpha$ with the membrane normal, $\hat{n}$. It is most convenient to express this in terms of the principal axes of the $Fe^{2+}$ zero field splitting tensor, $\hat{X}$, $\hat{Y}$ and $\hat{Z}$. With respect to these axes, $\hat{n}$ subtends an angle $\chi$ with $\hat{Z}$. In terms of the direction cosines relating $\hat{H}$ and $\hat{n}$ to the zero field splitting axes we have:

$$\boldsymbol{H} = |H|(\sin\theta\cos\phi, \sin\theta\sin\phi, \cos\theta) = |H|(k, l, m) \tag{8}$$

$$\hat{n} = (\sin\chi\cos\xi, \sin\chi\sin\xi, \cos\chi) = (k', l', m') \tag{9}$$

Here $\theta$ and $\phi$ are polar and azimuthal angles for $H$, while $\chi$ and $\xi$ are the analogous angles for $\hat{n}$ in the zero field splitting axis system. Now we can relate the angle $\alpha$ to $\theta$, $\phi$, $\chi$ and $\xi$ by setting $\alpha = \cos^{-1}[(\boldsymbol{H} \cdot \hat{n})/|\boldsymbol{H}|]$ yielding:

$$\alpha = \cos^{-1}(kk', ll', mm') \tag{10}$$

The probability for orientation $\alpha$ is $W(\alpha)$:

$$W(\alpha) = D'(\alpha) \sin\theta \tag{11}$$

where $D'(\alpha)$ is assumed to be a gaussian distribution, characterizing the orientation of the cells by

the aligning magnetic field. We have obtained $D'(\alpha)$ from the orientation dependence of the reaction center triplet EPR signal [19–21]. At 21 kG the distribution exhibits a spread of 0.4 radians about the aligning field. $D'(\alpha)$ equals unity for the random orientation case given in Eqn. 6. The intensity for a transition $i \rightarrow f$ at the Zeeman field $H$ is then:

$$I_{if}(H) = \int_0^{2\pi}\int_0^{2\pi} I_{if}(\theta,\phi)\, D'[\alpha(\theta,\phi,\chi,\xi)] \sin\theta \, d\theta \, d\phi \quad (12)$$

Eqn. 7 is then used to calculate the total intensity of all transitions. The integrated intensity over all fields is:

$$A = \int_0^{\infty} I(H) dH \quad (13)$$

The integral includes only $x$-band transitions within the field region observed experimentally.

## Results

*EPR in whole cells and chromatophores*

The maximum peak-to-through 'linewidth' of the iron-semiquinone EPR signal below $g' \approx 1.8$ is $270 \pm 30$ G in the ascorbate reduced sample for which only $Q_2$ is reduced (Fig. 3, top). This is an operational definition and not the intrinsic linewidth. This increases to 420 G in the dithionine-reduced sample, for which $Q_2$ is doubly reduced and hence diamagnetic, and $Q_1$ is singly reduced (Fig. 3, bottom). Partial reduction of the intermediate electron-acceptor bacteriopheophytin gives rise to additional EPR components, designated as $I^-$ in Fig. 3, under the weak preillumination used to insure complete reduction of the iron-quinone complex prior to freezing in the dark after 5 min. The same 420 G linewidth is observed if illumination is omitted during the incubation step, although an overall lower intensity is observed, owing to poorer equilibration with the dithionite plus methyl viologen. For unilluminated samples there is no $I^-$ reduction to mask the region above $g' = 1.8$ and the spectra reveal an additional peak at an effective $g'$ value of 2.11. This peak is found in the lower trace of Fig. 4. It appears to be a feature of $Q_1^- Fe^{2+}$ and is sensitive to the extent of membrane fractionation. For example, it appears in whole cells but not in chromatophores.

Fig. 4 also shows that there is a significant dependence of the EPR spectral intensity on the orientation of the membranes. This dependence is

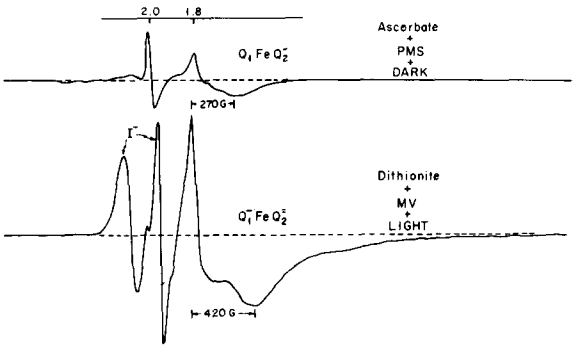


Fig. 3. EPR spectra of randomly oriented *Rps. viridis* whole cells for two reducing conditions as noted. All conditions refer to pretreatment of the samples prior to EPR observation in the dark at 12.5 K. The illuminated sample was dark-adapted for 5 min prior to freezing. Spectrometer conditions: microwave power, 150 mW; modulation amplitude, 32 G; frequency, 9.2 GHz.

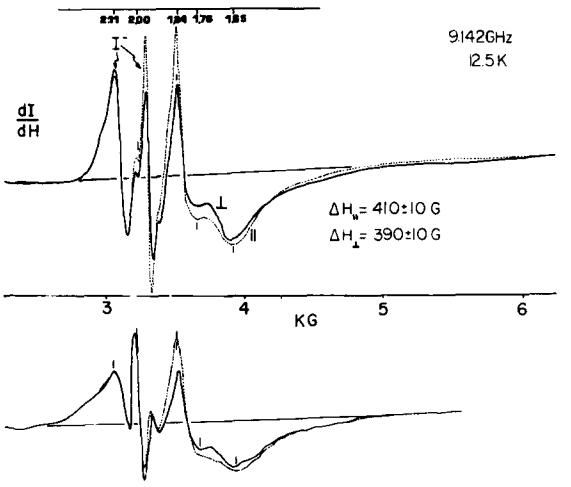


Fig. 4. EPR spectra of *Rps. viridis* whole cells which have been oriented by a 21 kG magnetic field prior to measurement. Top panel, sample conditions as in Fig. 2 lower trace. Bottom panel, sample was reduced with dithionite and methyl viologen in the dark. Solid trace refers to a perpendicular ( $\perp$ ) orientation of the EPR field relative to the direction of the aligning field, while the dashed trace refers to a parallel ($\parallel$) orientation. Spectrometer conditions as in Fig. 2.

unlike that encountered in the $g$-anisotropy of a single crystal of an isolated spin-$\frac{1}{2}$ particle, where the integrated intensity is preserved, and the resonance field shifts with alignment of the molecular axes along the EPR field. By contrast, the integrated intensity of the EPR spectrum in the $Q_1^- Fe^{2+} Q_2^{2-}$ state decreases by 25% in going from a parallel to a perpendicular alignment. The sharp peak at $g' = 1.84$ exhibits the highest dichroic ratio, $I_{\parallel}/_{\perp} I = 1.61$; for the $g' = 1.65$ peak it is only $I_{\parallel}/I_{\perp} = 1.09$.

The position of the peak at $g' = 1.84$ remains invariant with orientation. The peak at $g' = 1.65$ shifts by 30 G to lower field for the $\perp$ -orientation. The peak intensities vary smoothly with angle, peaking at the orientation when the long axis of the cell is perpendicular to the EPR magnetic field.

The lineshape of the iron-semiquinone signal in chromatophores is dramatically different from that found in whole cells, as noted in Fig. 5. For chromatophores, the sharp peak appears at $g' = 1.85$ and the linewidth is $195 \pm 20$ G in the dithionite-reduced samples. This is to be compared to the ascorbate-reduced sample where the spectrum exhibits two peaks below $g' = 1.85$, having breadths of $175 \pm 20$ G and $325 \pm 30$ G. There is no observable peak at $g' \approx 2.1$ as was found in the whole cells.

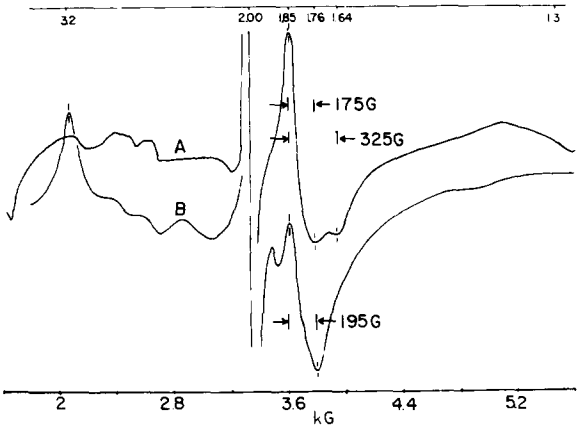


Fig. 5. EPR spectra of randomly oriented *Rps. viridis* chromatophores under reducing conditions. (A) Chromatophores in 0.025 M glycine buffer comprising 0.1 M KCl/0.01 M ascorbate/$10^{-5}$ M phenazine methosulphate at pH 10. (B) Chromatophores in glycine/KCl buffer, comprising 0.01 M dithionite/$10^{-5}$ M methyl viologen at pH 10. Temperature, 12.5 K; microwave power, (A) 100 mW and (B) 200 mW.

Although the lineshape of the iron-semiquinone signal depends upon the extent of reduction ($Q_1^- Fe^{2+} Q_2^{2-}$ vs. $Q_1 Fe^{2+} Q_2^-$) and the disruption of the membrane (whole cells vs. chromatophores and also reaction centers), the position of the sharp peak at $g' = 1.84$–$1.85$ is essentially invariant to such alterations. This feature is a hallmark of the iron-semiquinone complex.

The temperature dependence of the lineshape and of the peak intensity at $g' = 1.84$ (not shown) indicates that there is strong relaxation to the lattice, which abolishes the EPR signal above 20 K. The preferential loss of intensity with increasing temperature at resonance-field positions above and below the 1.84 peak indicates that this transition must lie lowest in energy or have significantly less coupling to the lattice than do the transitions giving rise to the features at other field positions.

*Spectral simulation*

The ratio of integrated intensities for parallel vs. perpendicular aligned cells $A_{\parallel}/A_{\perp}$, was calculated for a set of projections $\hat{Z} \cdot \hat{n} = 0.1$–$0.9$ (e.g., $\cos \chi = \hat{Z} \cdot \hat{n}$) and compared to our experimental value for oriented whole cells in order to determine the orientation of $Z$ with respect to $\hat{n}$. An axially symmetric distribution of orientations for the $\hat{Z}$ principal axis relative to $\hat{n}$ was assumed in this calculation. Thus, Eqn. 9 was reduced to orientation $(\sin \chi, 0, \cos \chi)$, and this corresponds to assuming equivalent projections of the $\hat{X}$ and $\hat{Y}$ zero field splitting axes on $\hat{n}$. In other words, we assume that there is no preferred orientation of the zero field splitting axes within the plane of the membrane; they are fixed only relative to the normal. No evidence exists on this issue. The results are given in Table I. We find that the experimental ratio of $A_{\parallel}/A_{\perp} = 1.25$ corresponds to the projection of $\hat{Z}$ along $\hat{n}$ of $\chi = 64 \pm 6°$. Thus, the axial ligand-field component of the iron ligand field is pitched at an angle of 26° from the membrane plane. The area ratio $A_{\parallel}/A_{\perp}$ is a sensitive function of $\chi$, increasing from unity at 90° to 2.5 at 26°. If the cell alignment was perfect and if $\hat{Z}$ was parallel to $\hat{n}$, then this intensity variation would also be a lower limit to that expected for $\theta$ decreasing from 90° to 26°. This orientation dependence of the intensity is primarily caused by the dependence of the wavefunction mixing be-

TABLE I

RATIO OF EPR-INTEGRATED AREAS FOR VARIOUS PROJECTIONS ($\chi$) OF THE $Z$ PRINCIPAL AXIS ON THE NORMAL TO THE MEMBRANE PLANE, $\hat{n}$

Using the *Rps. viridis* density of states at 21 kG and a spread of 0.4 radians [20].

| $\cos\chi$ | $\chi$ (in degrees) | $A_{\parallel}/A_{\perp}$ |
|---|---|---|
| 0.1 | 84 | 0.99 |
| 0.2 | 78 | 1.03 |
| 0.3 | 73 | 1.10 |
| 0.4 | 66 | 1.21 |
| 0.5 | 60 | 1.35 |
| 0.6 | 53 | 1.54 |
| 0.7 | 46 | 1.79 |
| 0.8 | 37 | 2.11 |
| 0.9 | 26 | 2.54 |

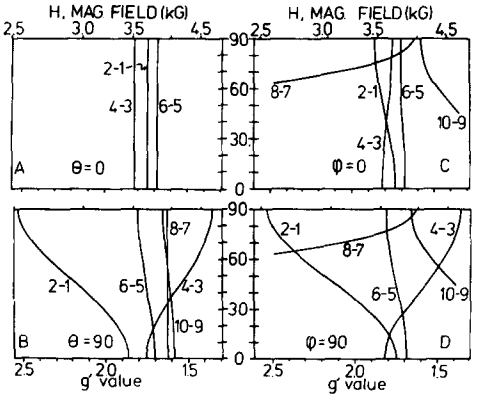


Fig. 6. Magnetic-field dependence as a function of orientation of the $Q^-Fe^{2+}$ X-band EPR transitions determined by numerical solution of the hamiltonian (Eqn. 1), as described in the text. Parameters: $D = 7.46\ cm^{-1}$, $E = 1.87\ cm^{-1}$, $J = 0.13\ cm^{-1}$, $g_Q = 2.0$, $g_z = g_x = g_y = 2.0$, $H_0 = 3270$ G. The magnetic field positions and the 'effective' $g'$ values for the transitions are given. The $g'$ value combines all sources of off-set from the isotropic free electron value by equating $g' = h\nu/\beta H'$. It is not the intrinsic $g$ value. A and B show the $\phi$ dependence at $\theta = 0°$ and 90°, respectively. C and D show that $\theta$ dependence at $\phi = 0°$ and 90°, respectively.

tween $Q^-$ and $Fe^{2+}$ on orientation(Appendix B).

It was possible to arive at a range of parameters for Eqn. 1 using the three fitting criteria presented earlier. In particular, we sought especially to learn how the spin-hamiltonian parameters might change when comparing spectra for $Q_1^-FeQ_2^{2-}$ vs. $Q_1FeQ_2^-$ or upon membrane fractionation. These parameters are directly related to the structure of the iron-semiquinone complex.

The magnetic field at which resonance occurs is predicted theoretically to depend significantly on the orientation of the iron principal axes relative to the applied field direction. Our results are presented in Fig. 6. The parameters chosen for this illustration include both axial and rhombic field components which yield a satisfactory fit to the spectrum. There are five transitions qualitatively described as semiquinone spin flips, which are pertubed by admixture with the five iron magnetic sublevels. Only the six lowest-energy levels in Fig. 2 are significantly populated below approx. 15 K, so that only the transitions designated 2–1, 4–3 and 6–5 in Fig. 5 could contribute to the spectra that we simulated. Fig. 6A shows that, when the magnetic field is parallel to the easy axis of magnetization ($Z$ axis, $\theta = 0$), the field positions of the three lowest transitions are independent of the projection of the rhombic field component of the iron ($\phi = 0$–$90°$). This must be so, since then $\hat{X}$ and $\hat{Y}$ have no projection on $\boldsymbol{H}$. Because the oscillator strength (Eqn. 2) is greatest when $\theta = 0$, we can expect these field positions to correspond to local maxima in the absorption curves and local crossing points in the derivative (experimental) curves.

The shift of all three transitions to low $g'$ values at $\theta = 0$, compared to that for a free semiquinone, can be readily explained. In the case of the 2–1 transition, the $Q^-$ wavefunction becomes admixed with a predominantly non-magnetic iron spin function, $M_s = 0$, which has no Zeeman interaction and $g' = 0$ to first order. The average $g'$ value is thus reduced. For the 4–3 and 6–5 transitions, the iron spin functions correspond to predominantly the symmetric and antisymmetric combination $|+2\rangle \pm |-1\rangle$. For purely rhombic symmetry fields, these are exact, and since $\langle S_Z \rangle = 0$ in such a field, again the Zeeman effect is partially quenched and $g'$ is reduced. The two highest transitions of Fig. 2, 8–7 and 10–9, do not fall within the surveyed range of 2–5 kG for these $\theta$ and $\phi$.

Fig. 6B shows that when $\hat{Z}$ is perpendicular to $\boldsymbol{H}$, there is a large divergence with $\phi$ for the 2–1 and 4–3 transition positions. A similar behavior is

observed when $\phi$ is fixed at 90° and $\theta$ is varied from 0° to 90° (Fig. 6D). This behavior can be readily understood in terms of an angle-dependent admixture of additional iron spin functions with the $Q^-$ spin functions. (We shall postpone a detailed discussion until we present analytical expressions for the transition energies in the next section.) We conclude from these results that between 7.5 and 20 K the $Q^-Fe$ EPR spectrum is the superposition of two and three transitions, respectively, which exhibit a high degree of anisotropy that can be attributed to a weak spin exchange interaction between the semiquinones and a low-symmetry, high-spin $Fe^{2+}$.

To extract the optimum parameters, a fit to the experimental derivative spectra was performed using the theory given in the last section. Simulated derivative spectra were obtained by evaluating $dI/dH$ from Eqn. 7. An example of one such simulation for $Q_1^- Fe^{2-} Q_2^{2-}$ is given in Fig. 7. The range of parameters which afford acceptable fits is given in Table II. These results indicate a narrow

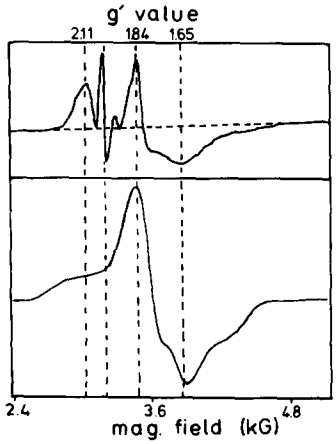


Fig. 7. Computer stimulation of the $Q^- Fe^{2+}$. EPR spectrum (bottom) compared to the experimental spectrum of $Q_1^- Fe^{2+} Q_2^{2-}$ (top). Parameters used for the fit: $D = 7.0\ cm^{-1}$; $E = 1.7\ cm^{-1}$, $J = 0.093\ cm^{-1}$, $g_\parallel = g_\perp = 2.00$, $\delta = 140$ G and $g_Q = 2.00$.

range of values for the splitting of the $Fe^{2+}$ quintet ground state. The magnitude of the axial distortion parameter $|D| = 7.0 \pm 0.13\ cm^{-1}$ is $\frac{1}{2}$–$\frac{2}{3}$ that

TABLE II

RANGE OF ACCEPTABLE PARAMETERS FOR SPIN HAMILTONIAN (Eqn. 1)

| | Numerical (in $cm^{-1}$) | Perturbation theory (Appendix C) (in $cm^{-1}$) | Major spectral influence |
|---|---|---|---|
| $Q_1^- Fe^{2+} Q_2^{2-}$ | | | |
| $\|D_1\|$ | 7.0 ±1.3 | 6.0 ±1.0 | Position of $g' = 1.84$ peak |
| $\|E_1\|$ | 1.7 ±0.5 | 1.0 ±0.2 | Position of $g' = 1.6$, 2.1 peaks |
| $\|E_1/D_1\|$ | 0.26 ±0.08 | 0.16±0.01 | – |
| $\|J_1\|$ | 0.12 ±0.03 | 0.52±0.12 | Same as $-\|E\|$ [b] and $\|D\|$ |
| $g_\parallel, g_\perp$ | 2.0 ±0.3 [a] | – | Little effect above 7.5 K, minor lineshape below 7.5 K |
| $g_Q$ | 2.00 [c] | 2.00 [c] | Position of all peaks |
| $\delta$ | 140 G | – | Gaussian intrinsic linewidth |
| $Q_1 Fe^{2+} Q_2^-$ | | | |
| $\|D_2\|$ | 7.0 [e] | 4.4 [d] | Position of $g' = 1.84$ peak |
| $\|E_2\|$ | 1.7 [e] | 1.0 [d] | Position of $g' = 1.6$, 2.1 peaks |
| $\|E_2/D_2\|$ | 0.26 [e] | 0.22±0.01 | – |
| $\|J_2\|$ | 0.06±0.003 [e] | 0.37 [d] | Same as $-\|E\|$ and $\|D\|$ |

[a] Upper limit set by typical $3d^6$ high-spin $Fe^{2+}$ examples.

[b] $|E|$ and $|J|$) have offsetting effects on the lineshape.

[c] Assumed identical to the free semiquinone.

[d] $E$ was fixed. Alternatively, if $J$ is fixed at 0.5 $cm^{-1}$, then $D = 5.8\ cm^{-1}$ and $E = 1.4\ cm^{-1}$ also fits.

[e] $D_2$ and $E_2$ were fixed at the $D_1$ and $E_1$ values, respectively, and $J_2$ was varied until a linewidth splitting of 270 G was obtained. These are not optimum parameters for a fit, as was evident from the poor agreement with the observed lineshape asymmetry for $Q_1 Fe^{2+} Q_2^-$. Alternatively, an increase in $E_2$ at constant $J_2$ will achieve a reduction in linewidth splitting which approaches 270 G. Agreement with the lineshape asymmetry was not achieved.

of typical hexacoordinate $Fe^{2+}$ complexes with nitrogen or oxygen donor ligands [28,29], and closer to that for tetracoordinate $Fe^{2+}$ with thiolate ligands ($D = 6.0\ cm^{-1}$, Ref. 30; $D = 7.7\ cm^{-1}$, Ref. 31).

The sign and symmetry of the axial distortion ($C_4$ vs. $C_3$ axial field) relative to the cubic field splitting could not be deduced from the spectrum. The $|E/D|$ ratio of $0.26 \pm 0.08$ indicates a significant rhombic character to the $Fe^{2+}$ ligand field. A ratio of $|E/D| = \frac{1}{3}$ indicates a purely rhombic distortion from cubic symmetry. Again, the sign and nature of the lower symmetry distortion ($C_2$ vs. $C_1$ axis) was not determinable.

Table II also shows that the exchange interaction is restricted to a narrow range, $|J| = 0.12 \pm 0.03\ cm^{-1}$ and is weak by comparison with thermal energies at room temperature ($212\ cm^{-1} = 300$ K). The sign of $J$ is positive, indicating that the interaction between $Q^-$ and $Fe^{2+}$ must be antiferromagnetic, provided that the axial field parameter $D$ is also assumed to be positive.

To accommodate the 36% reduction in the experimental linewidth observed in the ascorbate-reduced samples ($Q_1Fe^{2+}Q_2^-$), and simultaneously retain the $g' = 1.84$ resonance, it was necessary to decrease the value of $|J|$ by approximately the same extent while dropping $|D|$ at fixed $|E|$, thus increasing the rhombic character. This yielded a simulated spectrum with maximum at $g' = 1.84$ and a minimum at $g' = 1.71$ (not shown). These features are present in the experimental spectrum in Fig. 3. Within a limited range, the $|J|$ and $|E|$ parameters introduced off-setting effects on the positions of both a low-field and a high-field resonance ($g' \approx 2.1$ and 1.6). Thus, it was also possible to account for the $Q_2Fe^{2+}Q_2^-$ spectrum by assuming a smaller decrease of $|J|$, if $|E|$ was increased and $|D|$ was simultaneously decreased, so that again $|E/D|$ increased. In each case, the rhombic character of the $Fe^{2+}$ ligand field is greater for the $Q_1Fe^{2+}Q_2^-$ oxidation state.

The effects on the spectrum, as judged by the aforementioned three criteria, were systematically evaluated for all of the spin-hamiltonian parameters. $E$ and $J$ were found to exhibit off-setting shifts of the positions of the $g' \approx 1.6$ and $\approx 2.1$ peaks, while $J$, and predominantly $D$, rather than $E$ determined the position of the $g' \approx 1.84$ peak.

The $g$ value of $Q^-$ was fixed at the free semiquinone value of 2.004. The intrinsic $g$ value of the $Fe^{2+}$ had little effect on the spectral features for magnetic field up to 5000 G and for $T \geqslant 7.5$ K. The only spectral feature which was influenced by incrementing the iron $g$ factor between 2.3 and 1.7 was the 'nub' between the peaks at $g' = 1.84$ and $g' = 1.65$. The dependence is weak and disappears at higher temperatures, indicating that this parameter is best fit using lower temperatures than available in the present study (less than 7.5 K). The major spectral influence which each parameter exhibits is tabulated in Table II.

*Perturbation theory solution*

Although the numerical solutions given in the last section provide an accurate approach to solving the model hamiltonian (Eqn. 1), they do not yield analytical expressions for the eigenvalues, which would be extremely convenient in predicting the effects of changes in the parameters on the spectrum. For example, it would be very helpful to be able to deduce from observed spectral changes which parameters have changed upon membrane fractionation, binding of inhibitors such as *o*-phenanthroline, quinone removal and substitution and metal substitution. The nature of the alteration could then be characterized as affecting either $Fe^{2+}$, $Q^-$ or their mutual interaction.

A perturbation expansion of the matrix given in Appendix A is not suitable for this purpose, because on this basis the off-diagonal elements are not always very much smaller than the difference in diagonal terms. However, by first finding the iron spin functions which diagonalize the hamiltonian in Eqn. 1, excluding the $Q^-$ terms, this shortcoming is avoided. This extended method yields results which may be applied generally and should be useful for analyzing the Mössbauer spectrum of the $Fe^{2+}$. The matrix elements necessary for deriving the eigenvalues are given in Appendix III. The perturbation expressions for the three lowest transitions corresponding to the 2–1, 4–3 and 6–5 transitions are given in Table III. These also were used to predict the range of parameters which gave good fits to the spectrum. In this case a simulation was not performed, but instead prediction of both the first derivative resonances at $g' = 1.84$ and $g' = 1.65$ ($Q_1^-Fe^{2+}Q_2^{2-}$)

TABLE III

EPR TRANSITION ENERGIES CALCULATED BY A PERTURBATION EXPANSION (Appendix C) FOR $Q^- Fe^{2+}$

$G_Q = g_Q \beta H_0$, $a = \cos^2\alpha_1 - \sin^2\alpha_1$, $b = \cos\alpha_2 \sin\alpha_2$,

$\alpha_1 = \frac{1}{2}\tan^{-1}(6E/G_{\|}\cos\theta)$, $\alpha_2 = \frac{1}{2}\tan^{-1}(6E/DG_{\|}\cos\theta)$.

Only the dominant second-order terms are retained. Terms are evaluated in the following limits: $D \pm 3bE \pm G_Q m \gg (G_z m \pm J)a$; $\pi/4 \geq \theta \geq 0$.

In the limit $J \to 0$, where the result for an isolated, isotropic, $Q^-$ radical is expected, the remaining Zeeman term is still referenced to the iron axis system (Fig. 2) and not to the applied field direction. Hence, an apparent anisotropy remains in this limit which is not real and may be removed by transformation to an axis system which diagonalizes the Zeeman interaction (Ref. 25, p. 135).

| Assignment | Transition energy |
|---|---|
| 2–1 | $E_{0,\alpha} - E_{0,\beta} = G_Q(\cos\theta + \frac{1}{2}\tan\alpha\sin\theta) - 6J^2[\frac{\cos^2\alpha_1}{D+3bE-G_Q m} - \frac{\cos^2\alpha_2}{D-3bE+G_Q m} + \frac{\sin^2\alpha_2}{D-3bE-G_Q m} - \frac{\sin^2\alpha_1}{D+3bE+G_Q m}]$ |
| 4–3 | $E_{+1',\alpha} - E_{+1',\beta} = G_Q\cos\theta + 2aJ + \frac{(G_Q\sin\theta)^2}{2[G_Q\cos\theta + 2aJ]}$ |
| 6–5 | $E_{-1',\alpha} - E_{-1',\beta} = G_Q\cos\theta - 2aJ + \frac{(G_Q\sin\theta)^2}{2[G_Q\cos\theta - 2aJ]}$ |

or $g' = 1.71$ ($_1Fe^{2+}Q_2^-$) were judged to give acceptable parameters. The values of these parameters are tabulated in Table II. The acceptable range of values for $|D|$ is in near agreement with the numerical results. The rhombic parameter is reduced, $|E/D| = 0.16 \pm 0.01$, and the exchange interaction, $J_1 = 0.53 \pm 0.12$, is a factor of 4 larger, than the corresponding numerical results.

The equations for the transition energies in Table III correctly predict the trends in the numerically determined transition energies with $\theta$, $J$, $E$ and $D$. The angle dependence of the transitions given in Fig. 6c and d shows that as the angle between $\hat{Z}$ and $\boldsymbol{H}$ is increased from 0, the 2–1 transition shifts to lower field (higher effective transition energy), while the 4–3 transition shifts to higher field. The perturbation expressions for these transitions predict a $\theta$ dependence of $g_Q\beta H(\cos\theta + \frac{1}{2}\tan\theta\sin\theta)$ for the 2–1 transition, and, approximately, $g_Q\beta H\cos\theta$ for the 4–3 transition. These functions shift to lower field and higher field with increasing $\theta$, respectively, as numerically predicted. These perturbation solutions become increasingly unreliable for large $\theta$ ($\theta > \frac{1}{4}\pi$) and when $g_Q\beta H\cos\theta = 2aJ$. This strong angle dependence of the transition energies is partially the origin of the extremely broad lineshape, which extends most noticeably to high field and is characteristic of the $Q^- Fe^{2+}$ spectrum (Fig. 3). The physical origin of the orientation dependence of the transition energy arises from the competition for aligning the spin between $H$ and the direction of the internal magnetic field derived from the residual orbital angular momentum. The off-diagonal elements of $G_Q$ and $G_\perp$ in matrix (Eqn. C2) are responsible for this and result in the admixture of the spin functions for $Q^-$ and $Fe^{2+}$, respectively.

The position of the two lowest transitions at the turning point $\theta = 0$ is correctly predicted to be offset to higher magnetic fields compared to the free semiquinone. The 4–3 transition is correctly predicted to depend only on $J$ and $E$, and the 2–1 transition is correctly predicted to depend on $J$ and predominantly $D$ rather than $E$, for $|E/D| < 1/3$. The sign of $J$ does not influence the predicted position of the 2–1 transition. Also, because the 4–3 and 6–5 transitions are symmetric with respect to a sign change for $J$, the spectrum is predicted not to be dependent on the sign of $J$.

The 6–5 transition is predicted to lie to lower magnetic field, a feature which is not evident in the numerical solutions (Fig. 6). We attribute this to the importance of neglected terms arising from coupling to the higher-lying magnetic sublevels which become increasingly important as these states are approached in energy (Fig. 2).

To account for the reduced effective linewidth for the $Q_1Fe^{2+}Q_2^-$ oxidation state, the perturbation solutions also require an increase in the rhombic character from $|E/D| = 0.16$ to 0.22. This could be accomplished either by reducing $|J|$ and $|D|$ at fixed $|E|$, or by increasing $|E|$ and decreasing $|D|$ at fixed $|J|$.

In Table II it is apparent that the perturbation solutions for both redox states required exchange parameters that are a factor of 4–6 larger than the numerical results, while the zero field splitting of the iron is predicted to be smaller and more axial. In terms of our fitting criteria, these changes compensate one another, just as for the numerical results were $|E|$ and $|J|$ exhibit offsetting effects on the spectral features. These results illustrate the limitation in accuracy of the perturbation approach.

*Lineshape asymmetry*

The lineshape asymmetry of the $Q^-Fe^{2+}$ spectra appears to be caused only partly by the orientation dependence of the transition energies. The comparatively broader linewidth of the $g' = 1.65$ peak vs. the 1.84 peak and the sweeping tail at higher fields were not well simulated using hamiltonian (Eqn. 1) with a single intrinsic linewidth parameters (gaussian) or by including 10% $g$ anisotropy for $Fe^{2+}$ (Fig. 7). Nor was there explicitly evidence in the spectrum for resolved electron-electron dipolar splitting that might be a source of such lineshape asymmetry. However, by including a different intrinsic linewidth for each transition, which scaled as the dominant secular dipolar term, it was possible to selectively broaden the high-field side of the spectrum associated with the 4–3 transition (see Fig. 6) and, thereby, improve the fit. The 2–1 transition, which dominates the $g' = 1.84$ peak, can have no first-order dipolar splitting because $M_s$ is approx. 0 for the $Fe^{2+}$ in this transition, and hence a sharper resonance is predicted. The intrinsic linewidth used for the 2–1 transition was 140 G, which we attribute to all other unspecified sources of broadening, including a small spread in $|J|$. The additional gaussian linewidth for the 4–3 and 6–5 transitions was empirically estimated after all other parameters were fit by optimizing the ratio of peak height at $g' = 1.84$ to that at $g' = 1.65$ in the derivative spectra. With this restriction it was estimated that the addition linewidth was 100–200 G. It is possible to relate this to the average distance of separation between $Q^-$ and $Fe^{2+}$ using a simple point-dipole approximation for each spin. This is done in Appendix D and yields an estimated separation of $R = 6.2$–$7.8$ Å.

## Discussion

*Iron-semiquinone interaction*

The EPR data provide some answers about the electronic structure of the iron-semiquinone complex and its orientation within the membrane. The large anisotropy of the EPR intensity as a function or orientation observed in Fig. 4 is caused by the existence of a high degree of alignment of the ligand field around the iron. The axis of the largest ligand field component for iron is oriented at $26 \pm 6°$ from the plane of the photosynthetic membrane.

A proper picture of this complex is one in which the unpaired electron in the reduced state is essentially localized on either $Q_1^-$ or $Q_2^-$, the choice being governed by the extent of reduction – and includes weak orbital overlap with a low-symmetry $Fe^{2+}$. The biological significance of this interaction and the structure which fosters this coupling are of key interest. The magnitude of the exchange interaction $|J_1| \approx 0.12$ cm$^{-1}$ and $|J_2| = 0.06$ cm$^{-1}$ is significantly weaker than that observed for directly coordinated tris(orthosemiquinone)Fe(III) complexes 5 cm$^{-1}$ $< |J| <$ 300 cm$^{-1}$ (Ref. 32) and for 2-acetyl-1,4-semiquinone chelates with Mn(II) ($|J| \approx 200$ cm$^{-1}$, Ref. 33). In both cases the interaction is antiferromagnetic. No examples of Fe(II) $Q^-$ model complexes have been reported, evidently because the preferred equilibrium lies strongly towards the $Fe(II)Q^{2-}$ ground-state formulation [32]. Thus, there is extensive charge transfer between Fe(III) and coordinated semiquinones in model compounds. These observations

indicate strongly that there can be no direct coordination of the semiquinones by $Fe^{2+}$ in bacterial membranes. Nevertheless, the exchange interaction is an order of magnitude larger than that observed between the intermediate electron acceptor $BPh^-$ and $Q_1^-Fe^{2+}$ in *Rps. viridis* cells [12], and three orders of magnitude larger than that between $(BChl)_2^+$ and $I^-$ in $Fe^{2+}$-free reaction centers of *Rps. spheroides* and *R. Rubrum* [34]. The question arises as to what is the nature of the $Q^-Fe^{2+}$ interaction which fosters a comparatively strong coupling yet cannot be mediated by direct coordination? Evidently, it is not related to the chemical nature of the semiquinone, because the $g' = 1.8$ signal is observed in ubiquinone-extracted reaction centers of *Rps. spheroides* (R-26) which have been reconstituted with seven different quinones [35]. These observations suggest that the $Fe^{2+}$ may be coordinated by ligands having low-lying electronic states, capable of interacting with the metal valence electrons to transfer spin density to atomic centers away from the central metal. Semiquinones having binding sites adjacent to these coordinating ligands could be expected to exhibit an enhanced exchange interaction. This covalency would also explain the small $|D|$ value in comparison with typical hexacoordinate $Fe^{2+}$ complexes. Candidates for such ligands include aromatic and sulfur-containing amino acid residues of the reaction center. The EXAFS and X-ray absorption edge studies of reaction centers of *Rps. spheroides* (R-26) have been analyzed to show the involvement of roughly six second-row (C, N, O) ligands [16,17]. Anomalously large scattering from second and third shell atoms was interpreted to support the participation of imidazole or imidazolate ligands [17]. The latter would be a reasonable candidate for a covalent ligand capable of extensive spin delocalization.

In an EPR study of the interaction between square planar $Cu^{2+}$ and $VO^{2+}$ complexes coordinated to pyridyliminonitroxide radicals, Richardson and Kreilick [36] showed that strong antiferromagnetic coupling was supported ($|J| \approx 327$–$1000$ $cm^{-1}$) in the para-, meta- and ortho-substituted pyridines. These planar conjugated ligands have five, four and three atoms, respectively, between the metal atom and the nitroxide radical. Although the identity of the $Fe^{2+}$ ligands in reaction centers is unknown, we can expect physiological ligands such as histidine (imidazole), tyrosine and tryptophan to behave similarly to these models and thus be capable of transmitting spin density over similar distances to nearby semiquinones that are non-covalently bound.

*Dipolar interaction and linewidth*

Estimates of distance based on the magnitude of the exchange interaction are notoriously unreliable, because the relative orientation of the interacting orbitals within the superexchange pathways plays a crucial role in determining the magnitude and sign of the interaction [37]. The electron-electron dipolar interaction is not subject to such problems, and the point dipole approximation is a reliable estimate of the separation between the spin centers when their separation exceeds the size of the delocalized spins. A separation of 6.2–7.8 Å, calculated from an assumed dipolar broadening of the 4–3 transition, falls within this region for reliable estimates. This distance agrees nicely with the prediction of an intervening aromatic amino acid residue between $Fe^{2+}$ and $Q^-$ in the last section. Line broadening due to $g$ anisotropy alone of $Fe^{2+}$ within the interval $2.3 > g > 1.7$ could not reproduce the linewidth of this transition and affected primarily the position of the 'nub' between the peaks at $g' = 1.84$ and $g' = 1.65$.

Our assignment of the $g' = 1.65$ peak to primarily the 4–3 transition rather than the 2–1 transition is in apparent disagreement with the results of Feher and Okamura [1], who observe a peak at $g' = 1.67$ even at 2.1 K in their light-induced $Q^-Fe^{2+}$ signal in reaction centers of *Rps. sphaeroides* R-26 mutants. At this temperature there should be a factor of 10 lower population of the first excited doublet compared to the ground doublet for $Q^-Fe^{2+}$ in Fig. 2. This precludes this state from contributing at 2.1 K. Although inclusion of $g$ anisotropy for $Fe^{2+}$ in our simulations did broaden the transitions, this alone was unable to generate a peak at $g' = 1.65$ associated with the 2–1 transition. The 10% $g$ anisotropy for $Fe^{2+}$ deduced from magnetic susceptibility ($g_x = 2.15$, $g_y = 2.26$, $g_z = 2.03$, Ref. 7) also confirms this to be a small effect. The degree of $g$ anisotropy from $Fe^{2+}$ admixed into the $Q^-$ spin function will be even less. The possibility of sample heating by the

100 mW/cm$^2$ illumination used to generate the $Q^-Fe^{2+}$ signal in [1] should not be excluded as a potential source for this apparent discrepancy. Alternatively, this may represent a limitation imposed on our simulations by conducting the diagonalization at a fixed magnetic field strength, while experimentally the field is varied at fixed frequency.

*The spin hamiltonian parameters*

The $g'$ 1.8 EPR signal is a characteristic feature of the $Q^-Fe^{2+}$ complex in bacteriochlorophyl-*a* and -*b* type photosynthetic bacteria, including *Rps. sphaeroides, Chromatium vinosum, Rhodopseudomonas capsulata, Rhodopseudomonas palustris, Rhodopseudomonas gelatinosa,* and *Rps. viridis* [38]. The numerical solutions are consistent with and the perturbation expressions show that the position of this peak is a function of approx. $aJ^2[1/(D+\frac{3}{2}E)-1/(D-\frac{3}{2}E)]$. It is therefore evident that the $Q_1^-Fe^{2+}$ exchange interaction ($J_1$) must be conserved in the various organisms. The insensitivity of this peak to membrane fractionation encountered in the preparation of chromatophores and reaction centers indicates that the exchange interaction is not altered by such treatments. Additionally, changes in the rhombic ligand field component, $E$, are partially offsetting because it appears in both the numerator, $a = \cos^2\alpha_1 - \sin^2\alpha_1$, and the denominator. The $g' = 1.8$ transition is thus sensitive to $J$ and $D$ principally. By contrast, the linewidth is reduced appreciably upon membrane fractionation (compare Figs. 3 and 5). Because $E$ directly affects the position of the 4–3 transition (this transition depends on the product $aJ$), changes in the $Fe^{2+}$ rhombic field component could account for the linewidth dependence on membrane fractionation, while not affecting the position of the 1.8 peak. Dipolar coupling contributes predominantly to the lineshape asymmetry rather than to the position of the 4–3 transition. The appreciably shifted and narrowed $Q^-Fe^{2+}$ spectrum observed in *Rhodospirillum rubrum* [39] is probably caused by a different exchange interaction in this organism. The presence of the $g' = 1.84$ resonance for $Q^-Fe^{2+}$ in Photosystem II particles from *Chlamydomonas reinhardii* [40] indicates that the exchange interaction must be very nearly the same as in bacteria.

The magnitudes of the zero field splitting parameters for $Fe^{2+}$ determined in this work are, in principal, less reliably estimated than those obtained from experimental techniques which probe the $Fe^{2+}$ magnetic sublevels directly (for example, low-temperature magnetic susceptibility [7] and high-field Mössbauer spectroscopy). This is so because the magnetic sublevels of the $Fe^{2+}$ are not directly observed by EPR, but are sensed only through their perturbation of the $Q^-$ magnetic sublevels. Nevertheless, the requirement for an increased rhombic character for $Q_1Fe^{2+}Q_2^-$ vs. $Q_1^-Fe^{2+}Q_2^{2-}$ is real and is presumed to be caused by the additional build-up of charge on the quinones. This indicates that the quinones are geometrically disposed so as to either increase $|E|$ or decrease $|D|$ upon reduction. If the latter occurs,then it must also be true that $Q_2^-$ is exchange coupled more weakly than $Q_1^-$ (it should be noted that $Q_1^-Fe^{2+}Q_2^{2-}$ is a non-physiological state). This is consistent with the well-established enhanced chemical lability of $Q_2$ over $Q_1$ in reaction centers, although it is surely not the causative factor, because $kT \gg |J_1|$ or $|J_2|$. Determination of the geometry of the quinones with respect to the iron from the change in $|E/D|$ alone is not possible.

**Acknowledgements**

This work was supported by grants from the U.S. Department of Energy under contract DE-AC03-76SF00098 (Berkeley), the University of Connecticut Research Foundation and by the National Institutes of Health 5-R01-GM-28789-02 (Princeton).

**Appendix A**

The matrix of the spin hamiltonian (Eqn. 1) was evaluated on the direct product basis states comprised of the $Q^-$ spin functions, $\alpha$ and $\beta$, and the symmetrized combination of $S$, $M_s$ kets for the iron, $|2,1a\rangle = |1a\rangle = |+1\rangle - |-1\rangle$, $|2,1s\rangle = |1s\rangle = |+1\rangle + |-1\rangle$, etc. The resulting matrix is given below (vacant

elements are the hermitian conjugates).

| | $2^s\alpha$ | $2^s\beta$ | $2^a$ | $1^a\beta$ | $1^s\alpha$ | $1^s\beta$ | $1^a\alpha$ | $1^a\beta$ | $0\alpha$ | $0\beta$ |
|---|---|---|---|---|---|---|---|---|---|---|
| $2^s\alpha$ | $2D + \frac{1}{2}G_Q m$ | $\frac{1}{2}G_Q(k - il)$ | $2J + 2G_z m$ | 0 | $G_x k$ | $J$ | $-1G_y l$ | $-J$ | $2\sqrt{3}E$ | 0 |
| $2^s\beta$ | | $2D + \frac{1}{2}G_Q m$ | 0 | $-2J + 2G_z m$ | $J$ | $G_x k$ | $J$ | $-iG_y l$ | 0 | $2\sqrt{3}E$ |
| $2^a\alpha$ | | | $2D + \frac{1}{2}G_Q m$ | $\frac{1}{2}G_Q(k - il)$ | $-1G_y l$ | $-J$ | $G_x k$ | $J$ | 0 | 0 |
| $2^a\beta$ | | | | $2D - \frac{1}{2}G_Q m$ | $J$ | $-iG_y s$ | $J$ | $G_x k$ | 0 | 0 |
| $1^s\alpha$ | | | | | $-D + 3E + \frac{1}{2}G_Q m$ | $\frac{1}{2}G_Q(k - il)$ | $J + G_z m$ | 0 | $\sqrt{3}G_x k$ | $\sqrt{3}J$ |
| $1^s\beta$ | | | | | | $-D + 3E - \frac{1}{2}G_0 m$ | 0 | $-J + G_z m$ | $\sqrt{3}J$ | $\sqrt{3}G_x k$ |
| $1^a\alpha$ | | | | | | | $-D - 3E + \frac{1}{2}G_Q m$ | $\frac{1}{2}G_Q(k - il)$ | $-iG_y l$ | $-\sqrt{3}J$ |
| $1^a\beta$ | | | | | | | | $-D - 3E - \frac{1}{2}G_0 m$ | $\sqrt{3}J$ | $-iG_y l$ |
| $0\alpha$ | | | | | | | | | $-2D + \frac{1}{2}G_Q m$ | $\frac{1}{2}G_0(k - il)$ |
| $0\beta$ | | | | | | | | | | $-2D - \frac{1}{2}G_Q m$ |

$k = \sin\theta\cos\phi$, $G_x = g_x\beta H$, $G_Q = g_Q\beta H$
$l = \sin\theta\sin\phi$, $G_y = g_y\beta H$,
$m = \cos\theta$, $G_z = g_z\beta H$,

## Appendix B

Eqn. 2 was evaluated for each transition. A general expression for the transition probability can be written in terms of the ten basis functions,which comprise the eigenvectors obtained by solving Eqn. 1. The $|j\rangle$eigenvectors, $j = 1, 2, \ldots, 10$, have the form:

$$|j\rangle = C_{1j}|2s\alpha\rangle + C_{2j}|2s\beta\rangle + C_{3j}|2a\alpha\rangle + C_{4j}|2a\beta\rangle + C_{5j}|1s\alpha\rangle + C_{6j}|1s\beta\rangle + C_{7j}|1a\alpha\rangle + C_{8j}|1a\beta\rangle + C_{9j}|0\alpha\rangle + C_{10j}|0\beta\rangle$$

Here $C_{ij}$ is the coefficient for the $i$-th basis function in the $j$th eigenvector. Eqn. 2 is then:

$$W_{if} = \frac{H_1^2}{\hbar^2}\left|C_{1f}\left(\frac{g_Q}{2}k'C_{2i} - g_x k'C_{5i} + \frac{g_Q}{2i}l'C_{2i} + \frac{g_y}{i}l'C_{7i} + \frac{g_Q m'}{2}C_{1i} + 2g_z m'C_{3i}\right)\right.$$

$$+ C_{2f}\left(\frac{g_Q}{2}k'C_{1i} + g_x k'C_{6i} - \frac{g_Q}{2i}l'C_{1i} + \frac{g_y}{i}l'C_{8i} - \frac{g_Q}{2}m'C_{2i} + 2g_z m'C_{4i}\right)$$

$$+ C_{3f}\left(\frac{g_Q}{2}k'C_{4i} + g_x k'C_{7i} + \frac{g_Q}{2i}l'C_{4i} + \frac{g_y}{i}l'C_{5i} + \frac{g_Q}{2}m'C_{3i} + 2g_z m'C_{1i}\right)$$

$$\left. + C_{4f}\left(\frac{g_Q}{2}k'C_{3i} + g_x k'C_{8i} - \frac{g_Q}{2i}l'C_{3i} + \frac{g_y}{i}l'C_{6i} - \frac{g_Q}{2}m'C_{4i} + 2g_z m'C_{2i}\right)\right.$$

$$+C_{5f}\left(\frac{g_Q}{2}k'C_{6i}+g_xk'(C_{1i}+1.22C_{2i})+\frac{g_Q}{2i}l'C_{6i}-\frac{g_y}{i}l'C_{3i}+\frac{g_Q}{2}m'C_{5i}+g_zm'C_{7i}\right)$$

$$+C_{6f}\left(g_Qk'C_{5i}+g_xk'(C_{2i}+1.22G_{10i})-\frac{g_Q}{2i}l'C_{5i}-\frac{g_y}{i}l'C_{4i}-\frac{g_Q}{2}m'C_{6i}+g_zm'C_{8i}\right)$$

$$+C_{7f}\left(\frac{g_Q}{2}k'C_{8i}+g_xk'C_{3i}+\frac{g_Q}{2i}l'C_{8i}+\frac{g_v}{i}l'(1.22C_{9i}-C_{1i})+\frac{g_Q}{2}m'C_{7i}+g_zm'C_{5i}\right)$$

$$+C_{8f}\left(\frac{g_Q}{2}k'C_{7i}+g_xk'C_{4i}-\frac{g_Q}{2i}l'C_{7i}+\frac{g_y}{i}l'(1.22C_{10i}-C_{2i})+\frac{g_Q}{2}m'C_{8i}+g_zm'C_{10i}\right)$$

$$+C_{9f}\left(\frac{g_Q}{2}k'C_{10i}+g_xk'(2.45C_{5i})+\frac{g_Q}{2i}l'C_{10i}-\frac{g_y}{i}l'(2.45C_{7i})+\frac{g_Q}{2}m'C_{9i}\right)$$

$$+C_{10f}\left(\frac{g_Q}{2}k'C_{9i}+g_xk'(2.45C_{6i})-\frac{g_Q}{2i}l'C_{9i}-\frac{g_y}{i}l'(2.45C_{8i})-\frac{g_Q}{2}m'C_{10i}\right)\Bigg|$$

## Appendix C

*Perturbation theory expansion for $Q^-Fe^{2+}$*

The eigenvalues and eigenfunctions for the hamiltonian (Eqn. 1) excluding the $Q^-$ terms and the exchange interaction have been evaluated [26,28]. For either $\theta = 0$ or for small off-diagonal terms in $(G_\perp \sin\theta)^2/(D \mp 3E)$, the eigenfunctions for the $Fe^{2+}$ are approximately:

$$\begin{aligned}|+n'\rangle &= \cos\alpha|+n\rangle + \sin\alpha|-n\rangle \\ |-n'\rangle &= \sin\alpha|+n\rangle - \cos\alpha|-n\rangle\end{aligned} \tag{C1}$$

where $n = 1, 2$; for $n = 1$, $\alpha_1 = \frac{1}{2}\tan^{-1}(6E/G_{\|}\cos\theta)$; and for $n = 2$, $\alpha_2 = \frac{1}{2}\tan^{-1}(6E^2/DG_{\|}\cos\theta)$. We shall be interested only in the solutions near the turning points for which $\theta = 0$. The expressions developed here are appropriate to an axial $g$-tensor; however, inclusion of a rhombic $g$-tensor adds no new features. These eigenfunctions show that for $E \neq 0$ the solutions are non-symmetric admixtures of the $M_s$ doublets $\pm 1$ and $\pm 2$, found in axial symmetry.

Evaluation of the complete hamiltonian (Eqn. 1) for the coupled $Q^-Fe^{2+}$ system on the direct product basis obtained from Eqn. C1 and the two $Q^-$ functions yields the matrix Eqn. C2. On this basis the exchange interaction yields a diagonal contribution and a perturbation solution is valid in the aforementioned limits. The three lowest EPR transition energies, corresponding to 2–1, 4–3 and 6–5 in the notation of Fig. 6, were calculated using Eqn. C2 and are given in Table III.

| | $+2'\alpha$ | $+2'\beta$ | $-2'\alpha$ | $-2'\beta$ | $+1'\alpha$ | $+1'\beta$ | $-1'\alpha$ | $-1'\beta$ | $0\alpha$ | $0\beta$ |
|---|---|---|---|---|---|---|---|---|---|---|
| $+2'\alpha$ | $2D+2cJ$<br>$+\frac{1}{2}G_Qm$<br>$+2G_zmc$ | $\frac{1}{2}G_0n$ | $-4b(j+G_zm)$ | 0 | $G_1n$ | $2J\sin\alpha_1\sin\alpha_2$ | 0 | $2J\cos\alpha_1\sin\alpha_2$ | $\sqrt{6}\,E(\cos\alpha_2$<br>$+\sin\alpha_2)$ | 0 |
| $+2'\beta$ | | $2D-2cJ$<br>$-\frac{1}{2}G_Qm$<br>$+2G_zmc$ | 0 | $4b(J-G_zm)$ | $2J\cos\alpha_1\cos\alpha_2$ | $G_\perp n$ | $-2J\cos\alpha_1\sin\alpha_2$ | 0 | 0 | $\sqrt{6}\,E(\cos\alpha_2+$<br>$\sin\alpha_2)$ |
| $-2'\alpha$ | | | $2D-2cJ$<br>$-\frac{1}{2}G_Qm$<br>$-2G_zmc$ | $\frac{1}{2}G_Qn$ | 0 | $2J\sin\alpha_1\cos\alpha_2$ | $G_\perp n$ | $2J\cos\alpha_1\cos\alpha_2$ | $\sqrt{6}\,E(\cos\alpha_2$<br>$-\sin\alpha_2)$ | 0 |
| $-2'\beta$ | | | | $2D+2cJ$<br>$-\frac{1}{2}G_Qm$<br>$-2G_zmc$ | $-2J\cos\alpha_1\sin\alpha_2$ | $G_\perp n$ | $2J\sin\alpha_1\cos\alpha_2$ | $G_\perp n$ | 0 | $\sqrt{6}\,E(\cos\alpha_2$<br>$-\sin\alpha_2)$ |
| $+1'\alpha$ | | | | | $-D+3dE+aJ$<br>$\frac{1}{2}G_Qm$<br>$+G_zma$ | $\frac{1}{2}G_Qn$ | $2d(G_\perp m-J)$<br>$+3aE$ | 0 | $\frac{\sqrt{6}}{2}G_\perp n(\cos\alpha_1$<br>$+\sin\alpha_1)$ | $\sqrt{6}J\sin\alpha_1$ |
| $+1'\beta$ | | | | | | $-D+3dE-aJ$<br>$-\frac{1}{2}G_Qm$<br>$+G_zma$ | 0 | $2d(G_\perp m+J)$<br>$+3aE$ | $\sqrt{6}J\cos\alpha_1$ | $\frac{\sqrt{6}}{2}G_\perp n(\cos\alpha_1$<br>$+\sin\alpha_1)$ |
| $-1'\alpha$ | | | | | | | $-D-3dE-aJ$<br>$+\frac{1}{2}G_Qm-G_zma$ | $\frac{1}{2}G_Qn$ | $\frac{\sqrt{6}}{2}G_\perp n(\cos\alpha_1$<br>$-\sin\alpha_1)$ | $\sqrt{6}J\cos\alpha_1$ |
| $-1'\beta$ | | | | | | | | $-D-3dE+aJ$<br>$-\frac{1}{2}G_Qm$<br>$-G_zma$ | $-\sqrt{6}J\sin\alpha_1$ | $\frac{\sqrt{6}}{2}G_\perp n(\cos\alpha_1$<br>$-\sin\alpha_1)$ |
| $0\alpha$ | | | | | | | | | $-2D+\frac{1}{2}G_Qm$ | $\frac{1}{2}G_Qn$<br>$-2D-\frac{1}{2}G_Qm$ |
| $0\beta$ | | | | | | | | | | |

$a=\cos^2\alpha_1\text{-}\sin^2\alpha_1$, $c=\cos^2\alpha_2\text{-}\sin^2\alpha_2$, $m=\cos\theta$

$b=\cos\alpha_2\sin\alpha_2$ $d=\cos\alpha_1\sin\alpha_1$ $n=\sin\theta$.

The matrix is symmetric. (C2)

## Appendix D

The electron-electron dipolar interaction does not commute with the electron-spin exchange interaction and, as shown by Anderson [41], a dipolar broadened spectrum is narrowed by exchange coupling to yield an approximate expression for the half-width at half maximum:

$$\omega_{\frac{1}{2}} \approx \omega_{dd}^2/\omega_e \tag{D1}$$

where $\omega_{dd}$ is the frequency of the dipolar splitting and $\omega_e = J/\hbar$. For our system, the dominant secular term of the dipolar hamiltonian was used

$$\mathscr{H}_{dd} = \mathscr{D}(3S_{Qz}S_{Fez} - S_Q \cdot S_{Fe}) \tag{D2}$$

where $\mathscr{D} = g_Q g_{Fe}(1-3\cos^2\eta)/2\hbar R^3$

This is the only term which commutes with the Zeeman interaction and so is diagonal on the direct product basis states. The transitions between eigenfunctions obtained by solving the hamiltonian (Eqn. 1) are not characterized by constant values of $m_s$, $M_s$ and $S$. The later values are in fact orientation dependent. We thus estimated these only for the turning points in the spectrum at $\theta = 0$. The value of (Eqn. D2) was computed for each approximate eigenfunction using the basis states from Appendix C.

The final expression for the dipolar broadening using Eqns. D1 and D2 is then

$$\omega_{\frac{1}{2}} \approx \frac{\mathscr{D}^2[3 < S_{Qz} > < S_{Fez} > -2.875]^2}{J/\hbar}$$

Using the value $J = 0.13\ cm^{-1}$ we calculated the value of $\mathscr{D}$ from the estimates range of $\omega_{1/2} = 0.0047\ cm^{-1} - 0.0094\ cm^{-1}$ (50–100 G).

| Transition | $\lvert < S_{Qz} > \rvert$ | $\lvert < S_{Fez} > \rvert$ | $\mathscr{D}(cm^{-1})$ |
|---|---|---|---|
| 2– | $\frac{1}{2}$ | 0 | 0 |
| 4–3 | $\frac{1}{2}$ | $\cos^2\alpha_1 - \sin^2\alpha_1$ | 0.0063–0.0125 |
| 6–5 | $\frac{1}{2}$ | $\cos^2\alpha_1 - \sin^2\alpha_1$ | 0.0063–0.0125 |

## References


1 Feher, G. and Okamura, M.Y. (1979) Brookhaven Symp. Biol. 28, 183–194
2 Leigh, J.S. and Dutton, P.L. (1973) Annu. N.Y. Acad. Sci. 883–845
3 Parson, W.W. (1969) Biochim. Biophys. Acta 189, 384–396
4 Dutton, P.L., Prince, R.C. and Tiede, D.M. (1978) Photochem. Photobiol. 28, 939–949
5 Wraight, C.A. (1979) Photochem. Photobiol. 30, 767–776
6 Okamura, M.Y., Isaacson, R.A. and Feher, G. (1975) Proc. Natl. Acad. Sci. U.S.A. 72, 3491–3495
7 Butler, W.F., Johnson, D.C., Okamura, M.Y., Shore, H.B., Fredkin, D.R. and Feher, G. (1980) Biophys. J. 32, 967–992
8 Debrunner, P.G., Schultz, C.E., Feher, G. and Okamura, M.Y. (1975) Biophys. Soc. Abstr. 15, 226a
9 Boso, B., Debrunner, P.G., Okamura, M.Y. and Feher, G. (1981) Biochim. Biophys. Acta 638, 173–177
10 Wraight, C.A. (1978) FEBS Lett. 43, 283–288
11 Okamura, M.Y., Isaacson, R.A. and Feher, G. (1978) Biophys. Soc. Abstr. 21, 8a
12 Dismukes, C., Frank, H., Friesner, R. and Sauer, K. (1979) Biophys. Soc. Abstr. 25, 54a
13 Rutherford, A.W. and Evans, M.C.W. (1979) FEBS Lett. 100, 305–308
14 Rutherford, A.W. and Evans, M.C.W. (1979) FEBS Lett. 104, 227–230
15 Pucheu, N.L., Kerber, N.L. and Garcia, A.F. (1976) Arch. Microbiol. 109, 301
16 Eisenberger, P.M., Okamura, M.Y. and Feher, G. (1982) Biophys. J. 37, 523–538
17 Bunker, G., Stern, E.A., Blankenship, R.E. and Parson, W.W. (1982) Biophys. J. 37, 539–552
18 Eimhjellan, K.E., Aasmundrud, O. and Jensen, A. (1963) Biochim. Biophys. Res. Commun. 10, 232–236
19 Hales, B.J. and Das Gupta, A. (1979) Biochim. Biophys. Acta 548, 276–286
20 Frank, H.A., Friesner, R., Nairn, J.A., Dismukes, G.C. and Sauer, K. (1979) Biochim. Biophys. Acta 547, 484–501

21 Tiede, D.M. and Dutton, P.L. (1981) Biochim. Biophys. Acta 637, 278–290
22 Paillotin, G., Vermeglio, A. and Breton, J. (1979) Biochim. Biophys. Acta 545, 249–264
23 Oelze, J. and Drews, G. (1972) Biochim. Biophys. Acta 365, 209–239
24 Smith, B.T., Boyle, J.M., Dongarra, J.H., Garbow, B.S., Ikebe, Y., Klema, V.C. and Moler, C.B. (1976) Matrix Eigensystem Routines – EISPACK Guide, Springer, New York
25 Moriya, T. (1960) Phys. Rev. 120, 91–98
26 Abragam, A. and Bleany, B. (1970) Electron Paramagnetic Resonance of Transition Metal Ions, p. 209, Oxford University Press, Oxford
27 Friesner, R., Nairn, J.A. and Sauer, K. (1979) J. Chem. Phys. 71, 358–365 and 71, 5388
28 Tinkham, M. (1956) Proc. R. Soc. A 236, 535
29 Champion, P.M. and Sievers, A.J. (1977) J. Chem. Phys. 66, 1819–1825
30 Rubins, R.S. and Fetterman, H.R. (1979) J. Chem. Phys. 71, 5163–5166
31 Petrouleas, V., Simpoulos, A., Kostikas, A. and Coucouvanis, D. (1976) J. Phys. Coll. C6. 37, 159
32 Pierpont, C.G. and Buchanan, R.M. (1981) Coord. Chem. Rev. 38, 45–87
33 Mathur, P. and Dismukes, G.C. (1983) J. Am. Chem. Soc. 105, 7093–7097
34 Hoff, A.J., Gast, P., Isaacson, R. and Feher, G. (1981) in Photosynthesis III. Structure and Molecular Organization of the Photosynthetic Membrane (Akoyunoglou, G., ed.), pp. 1023–1029, Balaban International Science Services, Philadelphia, PA
35 Okamura, M.Y., Steiner, L.A. and Feher, G. (1974) Biochemistry 13, 1394–1403
36 Richardson, P.F. and Kreilick, R.W. (1978) J. Mag. Res. 29, 285–291
37 Hatfield, W.E. (1974) in Extended Interactions Between Metals, ACS Symposium 5 (Interrante, L.V., ed.), pp. 108–141, American Chemical Society
38 Clayton, R.K. and Sistrom, W.R. (1978) The Photosynthetic Bacteria, Plenum Press, New York
39 Prince, R.D. and Thornber, J.P. (1977) FEBS Lett. 81, 233–237
40 Nugent, J.H.A., Diner, B.A. and Evans, M.C.W. (1981) FEBS Lett. 124, 241–244
41 Anderson, P.W. and Weiss, P.R. (1953) Rev. Mod. Phys. 25, 269–276